



A Multiaxial Bionic Ankle Based on Series Elastic Actuation With a Parallel Spring

Shun Zhao , Wei Liang , Kunyang Wang , *Member, IEEE*, Lei Ren , *Member, IEEE*, Zhihui Qian , Guangrong Chen , Xuwei Lu , Di Zhao , Xu Wang , and Luquan Ren 

Abstract—Traditional robotic foot and ankle have received considerable attention for adaptive locomotion on complex terrain and land buffering ability. This study aims to develop a robotic ankle based on series elastic actuator with a parallel spring (SEAPS) by mimicking the two degree-of-freedom human ankle and related muscles. A unique four-SEAPS-based spring mechanism enhances motion adaptation and landing buffer. A dynamic model based on the SEAPS drive is presented, whereas a kinematic solution is realized. The bionic ankle has a wide range of motions with 30° in both the sagittal and frontal planes, which cover most of the human ankle motions. Four experiments were conducted to thoroughly characterize the capabilities. First, the static stiffness and the 2-D/3-D trajectory tracking performance of the proposed ankle were tested. Second, the angle sensing capacity under inclined road surface and the land buffering performance from a specific height were evaluated. The results show that the maximum 3-D motion tracking error is smaller than 2.3%, and the minimum sensing error of inclined road is smaller than 0.5%. The proposed ankle can closely track the 3-D walking trajectory of natural ankle joint with relative root-mean-square error well below 1.0%. Compared with no springs, landing buffer of the ankle with SEAPS can yield remarkable reduction in both peak ground reaction force (52.2%) and joint torque (57.9%). These findings prove that the SEAPS-based

bioinspired robotic ankle exhibits high land buffering performance in an unstructured environment, and also well reproduces the human-like movement in terms of complex 3-D ankle motions.

Index Terms—Bioinspired design, bionic ankle, land buffering, robotic foot, series-parallel elastic actuator.

I. INTRODUCTION

THE field of biorobotics—the construction of biologically inspired or bionic robots—takes inspiration from biological principles to design robots with sensorimotor skills that approach those of animals [1]. For robots, high adaptability on complex terrain requires not only wide range of motions at joints but also excellent landing performance on unstructured environment. In nature, many creatures achieve a stable landing cushion by controlling their body posture and muscle strength in real time when falling from high places [2], [3]. Researchers have studied the land buffering mechanisms of cats [4], toads [5], squirrels [6], and humans [7] to provide insights of bionic robotic designs. Particularly, when a person falls from a height or jumps to the ground, the cushioning stage is mainly realized by reallocating the flexion degree of the lower limb joints (hip, knee, and ankle), and adjusting the coactivation level of the flexor and extensor muscles around these joints [7], [8], [9].

Learning from that, robots can realize the landing cushion by changing the posture and adjusting the muscle force [10]. This has been first studied in the bioinspired jumping robots, where series elastic springs are attached to the knee [11] or hip [12] joints, acting as shock absorbers and energetic buffers. To date, the best cushioning performance of jumping robots is achieved by adding springs to the legs [13], but rarely through the ankles. However, the human ankle can achieve a distinct land buffering effect by controlling joint posture and muscle activation during many tasks [14], [15], [16]. So, researchers have then made efforts on bionic ankles to improve the cushioning effect by mimicking the musculoskeletal system of the human ankle. In the past several years, robotic ankle based on elastic actuators: series elastic actuator (SEA), parallel elastic actuator (PEA), and series elastic actuator with a parallel spring (SEAPS) have been successfully developed based on bionic principles [17], [18], [19], [20].

An elastic element gives a SEA unique properties compared to rigid actuators, including low output impedance, tolerance to impact loads, increased peak output power, and passive energy

Manuscript received 29 July 2022; revised 1 January 2023, 21 March 2023, 14 June 2023, and 28 July 2023; accepted 22 August 2023. This work was supported in part by the National Natural Science Foundation of China under Grant 52005209, Grant 91948302, Grant 91848204, and Grant 52021003, and in part by the Natural Science Foundation of Jilin Province under Grant 20210101053JC. (Corresponding authors: Kunyang Wang; Lei Ren.)

Shun Zhao, Wei Liang, Di Zhao, and Xu Wang are with the Key Laboratory of Bionic Engineering, Ministry of Education, Jilin University, Changchun 130025, China (e-mail: zhaoshun19@mails.jlu.edu.cn; weiliang@jlu.edu.cn; dizhao@jlu.edu.cn; wx19@mails.jlu.edu.cn).

Kunyang Wang, Lei Ren, Zhihui Qian, and Luquan Ren are with the Key Laboratory of Bionic Engineering, Ministry of Education, Jilin University, Changchun 130025, China, and also with the Institute of Structured and Architected Materials, Liaoning Academy of Materials, Shenyang 110167, China (e-mail: kywang@jlu.edu.cn; lren@jlu.edu.cn; zhqian@jlu.edu.cn; lqren@jlu.edu.cn).

Guangrong Chen is with the Robotics Research Center, Beijing Jiaotong University, Beijing 100044, China (e-mail: grchen@bjtu.edu.cn).

Xuwei Lu is with the Key Laboratory of Bionic Engineering, Ministry of Education, Jilin University, Changchun 130025, China, and also with the School of Mechanical, Aerospace, and Civil Engineering, University of Manchester, M13 9PL Manchester, U.K. (e-mail: xuwei.lu@manchester.ac.uk).

This article has supplementary material provided by the authors and color versions of one or more figures available at <https://doi.org/10.1109/TIE.2023.3310041>.

Digital Object Identifier 10.1109/TIE.2023.3310041

storage [21], [22]. A PEA consists of a driving element and an elastic element in parallel, and the common feature is that the force or torque required for controlling is jointly provided by the driving element and the elastic unit [23]. The PEA uses active control of the driving element to reasonably adjust the energy flow output of the paralleled passive elastic element, which can save energy, increase execution speed of tasks, and achieve static or dynamic balance of the system [24], [25]. The combination of SEA and PEA, forming SEAPS, has been widely used to increase the compliance and reduce motor requirements for the actuators [26], [27]. These elastic elements are often applied to one-degree-of-freedom (1-DOF) ankle to reduce the required motor torque [28], however, it faces difficulty to maintain balance when walking on uneven terrain or stepping on obstacles. Little is known about applying these actuators to 2-DOF active ankle.

The majority of biped robots walk on flat feet with 2-DOF ankles (e.g., HUBO [29] and Atlas [30]), but few of them are applied with elastic elements in both the sagittal and frontal planes. Several studies have applied active or passive elastic elements to the prosthetic ankles to assist amputee's walking and adapting on different terrains. Vinay et al. [31] developed a 2-DOF passive ankle-foot prosthesis by using adjustable parallel springs (PSs), and the amputee can alter the ankle to a preferred stiffness for various requirements. Jang et al. [32] presented a 2-DOF active ankle-foot prosthesis with a unique PEA-based mechanism, which can strengthen the propulsion of walking without increasing the mass. Agboola-Dobson et al. [33] used SEAPS in the design of a 2-DOF semiactive ankle, which was capable of providing not only sagittal plane motion and torque close to that of the human ankle but also adaptability to various sloped terrains. However, most of them concentrated on the motion performance on uneven terrains, little has published on using 2-DOF bionic ankle to improve the cushioning performance in complex environment.

This article attempts to address the land buffering problem of the existing robotics via a multi-axial bionic ankle. We propose a 2-DOF bionic robotic ankle composed of four SEAPSs that mimic the biomechanics of muscles surrounding human ankle, leading to excellent buffering performance in an unstructured environment. The contributions of this article are as follows.

- 1) Inspired from the interactions between the human agonistic and antagonistic muscles, we designed four SEAPSs around the bionic ankle to achieve the motions in dorsi/plantar flexion and inversion/eversion. Each of these four directions possessed a range of motion up to 30° covering most of the human ankle motion.
- 2) We established a kinematic model between the rotation angles of the motors and the ankle, to help the bionic ankle meet the 2-D/3-D motion tracking requirements and sense the angle of an inclined road surface with only motor encoders.
- 3) By combining the SEAPS (integrated from SEA and PS) with the multi-axial mechanism, the bionic ankle demonstrated good land buffering property on inclined road condition. During landing, the forces of SEA and PS are in opposite directions about the ankle center, resulting

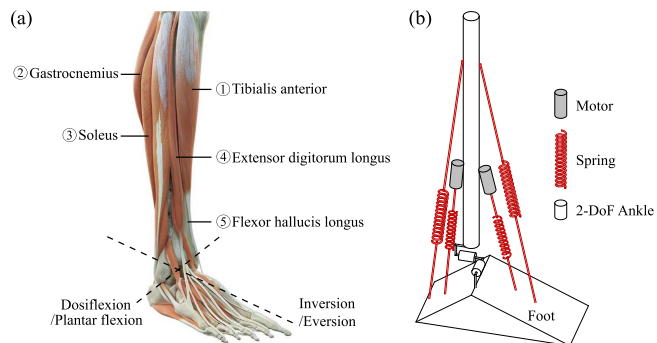


Fig. 1. Sketch of the bionic ankle. (a) Arrangements of the human ankle. (b) SEAPS units mimicking agonistic/antagonistic muscles in the sagittal plane.

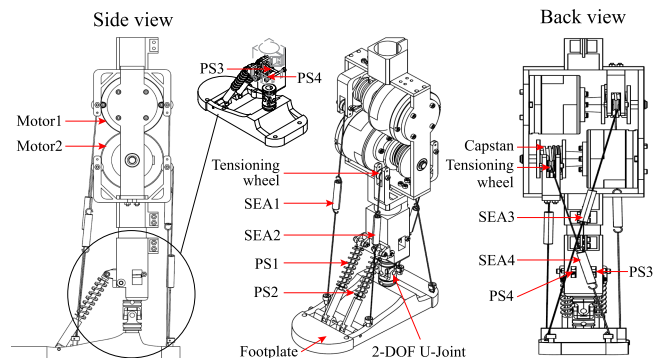


Fig. 2. Design of the bionic ankle based on four pairs of SEAPSs.

in significant reductions of the vertical ground reaction force (52.2%) and joint torque (57.9%).

The rest of this article is organized as follows. Section II introduces the design, kinematics, and dynamics of the proposed ankle. Section III describes the control strategy. Section IV presents the experimental cases. Finally, Section V concludes this article.

II. MECHANICAL SYSTEM

A. Bioinspired Design of the SEAPS

Design goals and specifications will be focused on the bionic ankle development. These specifications ensure that the bionic ankle with SEAPS units could effectively mimic the mechanics of its biological counterpart, particularly for joint and related muscles with distinct buffering ability (see Fig. 1). In human ankle, tibialis anterior and gastrocnemius/soleus are a pair of agonistic and antagonistic muscles for dorsi/plantar flexion, while flexor hallucis longus and extensor digitorum longus are a pair of agonistic and antagonistic muscles for inversion/eversion. Therefore, four pairs of active and passive muscles are formed into four SEAPSs in this study. Four active muscles SEAs were placed on the lower leg to obtain the 2-DOF ankle motions, with their passive muscles (PSs) anchored around the ankle for shock absorption and posture maintenance (see Fig. 2). This allows the SEAPSs to be tightly aligned on the bionic ankle, further achieving plantar flexion, dorsiflexion, inversion, and eversion.

TABLE I
SPECIFICATIONS AND PARAMETERS

Items	Specification
Total DOF	2-DOF
Weight(kg)	2.60
Height/length (m)	0.33/0.20
Range of Motion (°)	Dorsi/plantar flexion: ± 30 Inversion/eversion: ± 30
Maximum Speed (°/s)	Dorsi/plantar flexion: 315 Inversion/eversion: 495
Maximum Torque (Nm)	9.31
Spring Structure	SEAPS
SEA Resolution (bit)	7.7
Minimum control torque (Nmm)	0.45

- 1) *Dorsiflexion*: SEA1 and SEA2 mimic ① tibialis anterior muscle as the active dorsiflexor of the ankle. Parallel spring PS1 and PS2 mimic ② gastrocnemius as passive muscles.
- 2) *Plantar Flexion*: SEA3 and SEA4 mimic ③ soleus muscle as the active plantar flexor of the ankle joint. PS3 and PS4 mimic ① tibialis anterior muscle as the passive muscle.
- 3) *Inversion*: SEA1 and SEA4 mimic ④ extensor digitorum longus as the active invertors of the ankle. PS1 and PS4 mimic ⑤ flexor hallucis longus as the passive muscle.
- 4) *Eversion*: SEA2 and SEA3 mimic ⑤ flexor hallucis longus as the active evertors of the ankle. PS2 and PS3 mimic ④ extensor digitorum longus as the passive muscle.

B. Mechanical Structure of the Bionic Ankle

The bionic ankle comprises two brushless direct current motors (RMD-L-7025), two capstans, four SEAPSs (SEA1 and PS1, SEA2 and PS2, SEA3 and PS4, SEA4 and PS3), a 2-DOF U-joint, a footplate, and a tensioning system containing four pulley wheels. Two motors connect the capstans located at the top of the lower leg, which transmit power to the surrounding part of the foot frame through parallel SEAs. According to the peak moment and power of the human ankle joint during normal walking (1.5 Nm/kg and 2.88 W/kg) [34], we selected the motor parameters (1.6 Nm, 1500 r/min, 200 W). In addition, each SEAPS unit (SEA and PS) simulates the stiffness proportion of corresponding antagonistic muscles surrounding human ankle.

One end of each SEA is connected to a capstan, the other end is connected to the footplate using stainless steel cylinders, and the middle is supported by a tensioning wheel. The compact tensioning system is used to tighten ropes. Cylindrical pairs are connected to PSs, enabling the PSs to slide when the ankle is in inversion/eversion which further achieves the 3-D ankle rotation. The motion of the mechanism is realized using a combination of cylindrical pairs and universal joint (U-Joint). The main parameters are shown in Table I. The range of motion (RoM) in both the sagittal and frontal planes is set to $\pm 30^\circ$, as it covers most of the human ankle motions [34] and is easy for control.

C. Kinematic Analysis

A kinematic model is developed for controlling the ankle motion (see Fig. 3), which describes the relations between the foot posture and two motor angular displacements. The 2-DOF ankle

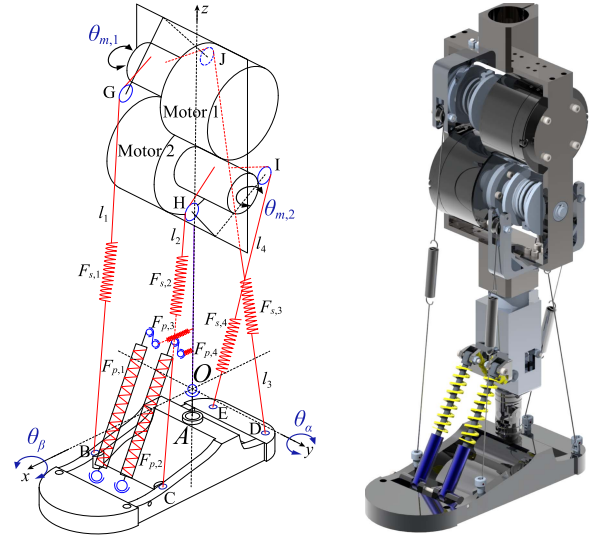


Fig. 3. Schematics and prototype model of the bionic ankle.

center (i.e., center of the universal joint) is defined as the origin of the global coordinate system O (i.e., the leg component). $\theta_{m,1}$ and $\theta_{m,2}$ indicate the rotation angles of the two motors in O . Four contact points of the SEAs (G, H, I, and J) are fixed in O and each point is described as $u_i \in \mathbb{R}^3$. The rotation angles of the bionic ankle are specified as θ_α (dorsiflexion/plantar flexion in the sagittal plane) and θ_β (inversion/eversion in the horizontal plane) in the local coordinate system A (i.e., the footplate). The other four contact points of the SEAs fixed on the footplate (B, C, D, and E) are described as $v_i \in \mathbb{R}^3$ in the local frame A . The origin of the local frame is same as the global frame.

For a given θ_α and θ_β , the rotation matrix $R_{O/A}$ is used to transform the local coordinates of points B, C, D, and E into the global coordinates. The rotation matrix R_{θ_α} in the sagittal plane and R_{θ_β} in the frontal plane comprise the $R_{O/A}$ as

$$R_{O/A} = R_{\theta_\alpha} \cdot R_{\theta_\beta} = \begin{pmatrix} 1 & 0 & 0 \\ 0 & \cos \theta_\alpha & -\sin \theta_\alpha \\ 0 & \sin \theta_\alpha & \cos \theta_\alpha \end{pmatrix} \begin{pmatrix} \cos \theta_\beta & 0 & \sin \theta_\beta \\ 0 & 1 & 0 \\ -\sin \theta_\beta & 0 & \cos \theta_\beta \end{pmatrix}. \quad (1)$$

Then, the length change of the SEAs l_s can be calculated as

$$l_s = T(u_i, R_{O/A}, v_i) = t(\theta_\alpha, \theta_\beta) \quad (2)$$

where function T transforms contact point v_i into O by $R_{O/A}$ and then calculates the distance between u_i and v_i in O . As points u_i and v_i can be measured in the model and $R_{O/A}$ is only related to θ_α and θ_β , l_s can be then obtained by a function t , which consists of two variables (only ankle rotation angles θ_α and θ_β). Based on the geometric relations, the desired rotation angle of the n th motor $\theta_{m,n}$ can be estimated as follows:

$$\theta_{m,n} = \frac{360l_{s,i}}{\pi d} = \frac{360f_i(\theta_\alpha, \theta_\beta)}{\pi d} = c \cdot f_i(\theta_\alpha, \theta_\beta) \quad (3)$$

where $l_{s,i}$ is the length change of SEA i according to different postures, f_i is the function between $l_{s,i}$ and ankle angles (θ_α

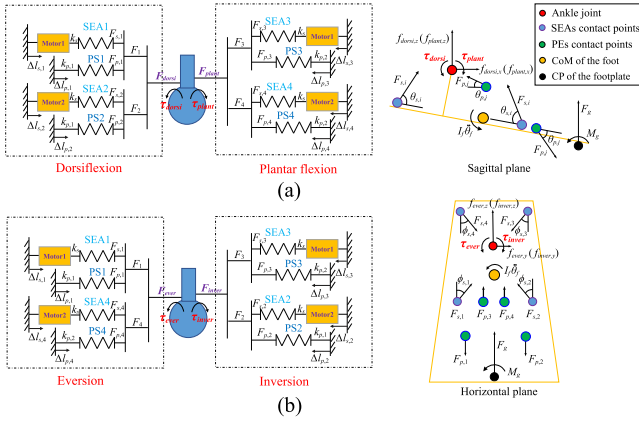


Fig. 4. Dynamic modeling of dorsi/plantar flexion in the sagittal plane (a) and inversion/eversion in the horizontal plane (b). F_{dorsi} / τ_{dorsi} , F_{plant} / τ_{plant} , F_{ever} / τ_{ever} , and F_{inver} / τ_{inver} : ankle joint force/torque under dorsiflexion, plantar flexion, eversion, and inversion, respectively. F_i : equivalent tendon driven force of SEAPS i . $f_{\text{dorsi},x}$, $f_{\text{plant},z}$, $f_{\text{ever},z}$, and $f_{\text{inver},z}$: joint forces in the z -direction under dorsiflexion, plantar flexion, eversion, and inversion, respectively. $f_{\text{dorsi},x}$ and $f_{\text{plant},x}$: joint forces in the x -direction under dorsiflexion and plantar flexion, respectively. $f_{\text{ever},y}$ and $f_{\text{inver},y}$: joint forces in the y -direction under eversion and inversion, respectively. $F_{s,i}$ and $F_{p,j}$: contraction forces of SEA i and PS j , respectively. F_g : vertical ground reaction force on the footplate. M_g : ground reaction moment on the footplate. k_s : stiffness of SEA. $k_{p,1}$: stiffness of PS1 and PS2. $k_{p,2}$: stiffness of PS3 and PS4. $\Delta l_{s,i}$ and $\Delta l_{p,j}$: spring deformations of SEA i and PS j , respectively. $\theta_{s,i}$ and $\theta_{p,j}$: vertical angles of SEA i and PS j , respectively. $\phi_{s,i}$: horizontal angle of SEA i . I_f and $\ddot{\theta}_f$: rotational inertia and angular acceleration of the footplate, respectively. CoM, center of mass; CP, contact point.

and θ_β), d is the diameter of the capstan connecting to each of the two motors, and c is a constant that equals to $360/(\pi d)$. It should be noted that the relation between the number i and n is different when the motor rotation angle is positive or negative.

Finally, the relations between the ankle angles and the motor angles of the bionic ankle can be expressed. The results show that the angle ranges of θ_α (dorsiflexion/plantar flexion) and θ_β (inversion/eversion) are -30° – 30° driven by two motors $\theta_{m,1}$ and $\theta_{m,2}$ with a rotation range of -220° – 160° .

D. Dynamic Analysis

The dynamics of the bionic ankle are then mathematically modeled in Fig. 4, and each motion of dorsiflexion/plantar flexion and inversion/eversion is applied using two SEAs and their corresponding PSs. The muscle forces generated by the i th SEA $F_{s,i}$ and the j th PS $F_{p,j}$ are described as follows:

$$\begin{cases} F_{s,i} = k_s \Delta l_{s,i} + F_T \\ F_{p,j} = k_p \Delta l_{p,j} \end{cases} \quad (4)$$

where F_T is the preload force of the SEAs, $\Delta l_{s,i}$ and $\Delta l_{p,j}$ are the spring deformation of the SEA i and PS j , respectively. When the bionic ankle is in the initial position, the preload forces F_T of the four SEA muscles are equal to ensure ankle balance.

Different postures in the sagittal and frontal planes are driven by different SEAPS (see Fig. 4). The ankle joint forces and torques were calculated under different postures. It was assumed that the force directions of SEA1, SEA2, and four PSs were

parallel to the sagittal plane, while the directions of SEA3 and SEA4 were parallel to the frontal plane. The muscles involved in dorsiflexion are SEA1, SEA2, PS1, and PS2, so the ankle joint forces f_{dorsi} and torques τ_{dorsi} in dorsiflexion are calculated as

$$\begin{cases} f_{\text{dorsi},x} = \sum_{j=1,2} F_{p,j} \cos \theta_{p,j} - \sum_{i=1,2} F_{s,i} \cos \theta_{s,i} \\ f_{\text{dorsi},z} = \sum_{j=1,2} F_{p,j} \sin \theta_{p,j} - \sum_{i=1,2} F_{s,i} \sin \theta_{s,i} \end{cases} \quad (5)$$

$$\begin{aligned} \tau_{\text{dorsi}} = I_f \ddot{\theta}_f + \sum_{i=1,2} F_{s,i} r_{s,i} \cos \phi_{s,i} + f_{\text{dorsi},x} r_z \\ + f_{\text{dorsi},z} r_x + F_g r_g + M_g - \sum_{j=1,2} F_{p,j} r_{p,j} \end{aligned} \quad (6)$$

where $r_{s,i}$ and $r_{p,j}$ denote the moment arms of SEA i and PS j to the center of mass (CoM) of the foot; r_z and r_x denote distances between the ankle center and the CoM of the foot along the z and x axes; r_g denotes the moment arm at the contact point (CP) of the footplate to the CoM of the foot. It should be noted that the moments are described as scalar components along the corresponding axes which are resolved from the 3-D vectors.

Plantar flexion involves SEA3, SEA4, PS3, and PS4, so the ankle joint forces f_{plant} and torques τ_{plant} are calculated as

$$\begin{cases} f_{\text{plant},x} = \sum_{i=3,4} F_{s,i} \cos \theta_{s,i} - \sum_{j=3,4} F_{p,j} \cos \theta_{p,j} \\ f_{\text{plant},z} = \sum_{i=3,4} F_{s,i} \sin \theta_{s,i} + \sum_{j=3,4} F_{p,j} \sin \theta_{p,j} \end{cases} \quad (7)$$

$$\begin{aligned} \tau_{\text{plant}} = I_f \ddot{\theta}_f - \sum_{i=3,4} F_{s,i} r_{s,i} \cos \phi_{s,i} + f_{\text{plant},x} r_z \\ + f_{\text{plant},z} r_x + F_g r_g - M_g - \sum_{j=3,4} F_{p,j} r_{p,j} \end{aligned} \quad (8)$$

Eversion involves SEA1, SEA4, PS1, and PS4, so the ankle joint forces f_{ever} and torques τ_{ever} are calculated as

$$\begin{cases} f_{\text{ever},y} = \sum_{i=1,4} F_{s,i} \cos \theta_\beta - \sum_{j=1,4} F_{p,j} \cos \theta_\beta \\ f_{\text{ever},z} = \sum_{i=1,4} F_{s,i} \sin \theta_\beta - \sum_{j=1,4} F_{p,j} \sin \theta_\beta \end{cases} \quad (9)$$

$$\begin{aligned} \tau_{\text{ever}} = I_f \ddot{\theta}_f - \sum_{i=1,4} F_{s,i} r_{s,i} \sin \theta_\beta - f_{\text{ever},y} r_z + f_{\text{ever},z} r_y \\ + F_g r_g + M_g - \sum_{j=1,4} F_{p,j} r_{p,j} \sin \theta_\beta \end{aligned} \quad (10)$$

where r_y denotes the distance between the ankle joint and the center of mass of the ankle along the y -axis. Inversion involves SEA2, SEA3, PS2, and PS3, so the ankle joint forces f_{inver} and torques τ_{inver} are calculated as

$$\begin{cases} f_{\text{inver},y} = \sum_{j=2,3} F_{p,j} \cos \theta_\beta - \sum_{i=2,3} F_{s,i} \cos \theta_\beta \\ f_{\text{inver},z} = \sum_{i=2,3} F_{s,i} \sin \theta_\beta - \sum_{j=2,3} F_{p,j} \sin \theta_\beta \end{cases} \quad (11)$$

$$\begin{aligned} \tau_{\text{inver}} = I_f \ddot{\theta}_f + \sum_{i=2,3} F_{s,i} r_{s,i} \sin \theta_\beta + f_{\text{inver},y} r_z + f_{\text{inver},z} r_y \\ + F_g r_g + M_g + \sum_{j=2,3} F_{p,j} r_{p,j} \sin \theta_\beta \end{aligned} \quad (12)$$

This section introduces the bioinspired structure design and two mathematical models of the bionic ankle. The kinematic model provides theoretical support for joint motion control and ankle joint sensing, while the dynamic model calculates ankle

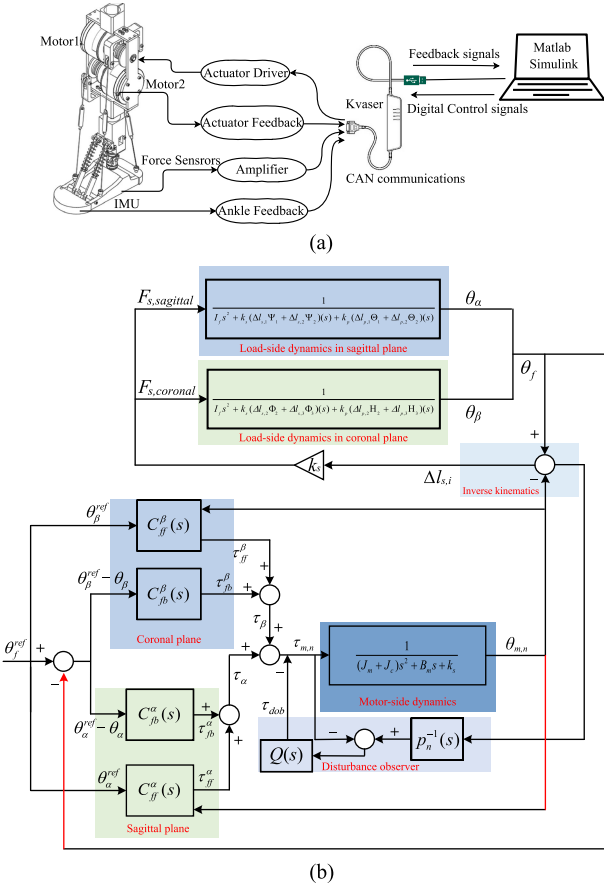


Fig. 5. Control system of the bioinspired foot. (a) Hardware connection mode. (b) Block diagram of the impedance controller.

joint forces and moments in order to control the joint motion at high level and evaluate the buffering performance when the bionic ankle lands on the ground.

III. CONTROL SYSTEM

This study uses Simulink (MATLAB, USA) for parameter processing of the control system [see Fig. 5(a)]. By using a communication module Kvaser (USB to CAN interface, 1 Mb/s output rate, 100- μ s intervals), the control parameters processed by Simulink can be timely transmitted to the CAN bus controller of the motors, while the feedback values of the motor encoder can be recorded and transmitted in turn. During the test of falling from a given height to the inclined platform, a thin-film pressure sensor (RP-C18.3-LT) is used to disable the motors when the footplate touches the platform. This makes the foot completely cover the road surface, and the sensor is only used as a switch to guide the ankle posture during the landing tests. The use of this pressure sensor is only necessary for the experiment. The IMU on foot is used to calculate ankle angle feedback for joint motion tracking. A data acquisition module (analogue input, C-7017) transmits the data collected by the sensors to Kvaser.

In this study, an impedance controller consisting of inverse dynamics feedforward controller, PD feedback controller, motor-side dynamics model, load-side dynamics model, and

disturbance observer (DOB) was used to generate ankle joint motions. The motor-side dynamics can be derived based on the output shaft of the motor as follows:

$$\tau_{m,n} = (J_m + J_c)\ddot{\theta}_{m,n} + B_m\dot{\theta}_{m,n} + k_s \left(\frac{\theta_{m,n}}{c} - f_i(\theta_f) \right) \quad (13)$$

where $\tau_{m,n}$, $\ddot{\theta}_{m,n}$, $\dot{\theta}_{m,n}$ represent the torque, angular acceleration, and angular velocity of the n th motor, respectively, J_m and J_c are the inertias of the motor and the capstan, B_m is the viscous friction coefficient of the motor, and θ_f is the 3-D ankle angle.

The relationships between the inputs and outputs can be calculated as transfer functions on the basis of the block diagram shown in Fig. 5. $P_m(s)$ describes the transfer function of the motor-side dynamics

$$P_m(s) = \frac{1}{(J_m + J_c)s^2 + B_ms + k_s}. \quad (14)$$

Then, the control model of the joint can be analyzed in three dimensions. For instance, a 3-D ankle joint motion containing both sagittal dorsiflexion and coronal inversion were analyzed as follows. Relationship between the SEA and PS springs deformation with the motor and ankle angles can be described as

$$\begin{cases} \Delta l_{s,i} = \theta_{m,n}/c - f_i(\theta_f) \\ \Delta l_{p,j} = R_p^{-1}(\theta_f)r_{p,j} \end{cases} \quad (15)$$

where $R_p^{-1}(\theta_f)$ is the inverse of the rotation matrix with the PS and the bionic ankle. Dynamics of the ankle dorsiflexion in the sagittal model is described as

$$\begin{cases} r_{s,i} \cos \phi_{s,i} - \cos \theta_{s,i}r_z - \sin \theta_{s,i}r_x = \Psi_i(\theta_\alpha) \\ \cos \theta_{p,j}r_z + \sin \theta_{p,j}r_x - r_{p,j} = \Theta_j(\theta_\alpha) \end{cases} \quad (16)$$

where $\Psi(s)$ and $\Theta(s)$ are the moment arms of SEA and PS projected in the sagittal plane. Ankle joint torques in dorsiflexion posture is simplified as follows:

$$\begin{aligned} \tau_{\text{dorsi}} = & I_f \ddot{\theta}_f + \sum_{i=1,2} \left(k_s \left(\frac{\theta_{m,n}}{c} - f_i(\theta_f) \right) + F_T \right) \Psi_i(\theta_\alpha) \\ & + \sum_{j=1,2} k_p R_p^{-1}(\theta_f)r_{p,j} \Theta_j(\theta_\alpha) + F_g r_g + M_g \end{aligned} \quad (17)$$

$P_{l,\text{dorsi}}(s)$ describes the transfer function of the load-side dynamics in dorsiflexion posture as

$$P_{l,\text{dorsi}}(s) = \frac{1}{I_f s^2 + k_s (\Delta l_{s,1} \Psi_1 + \Delta l_{s,2} \Psi_2)(s) + k_p (\Delta l_{p,1} \Theta_1 + \Delta l_{p,2} \Theta_2)(s)}. \quad (18)$$

The control for the dorsiflexion consists of a feedback controller $C_{fb}^\alpha(s)$ and a feedforward controller $C_{ff}^\alpha(s)$, as shown in Fig. 5(b). The feedforward controller is consisted with (18). The feedback controller adopts proportional-derivative (PD) controller according to the difference between the target value and the actual value.

Ankle joint torques in inversion posture is described as

$$\tau_{\text{inver}} = I \ddot{\theta}_f$$

$$\begin{aligned}
& + \sum_{i=2,3} F_{s,i} \sqrt{(r_{s,i} + r_y)^2 + r_z^2} \sin(\theta_\beta - \arctan r_z / r_{s,i} + r_y) \\
& + \sum_{j=2,3} F_{p,j} \sqrt{(r_z + r_{p,j})^2 + r^2} \cos(\theta_\beta + \arctan r / r_z + r_{p,j}) \\
& + F_g r_g + M_g \quad (19) \\
& \left\{ \begin{aligned} \sqrt{(r_{s,i} + r_y)^2 + r_z^2} \sin(\theta_\beta - \arctan r_z / r_{s,i} + r_y) &= \Phi_i(\theta_\beta) \\ \sqrt{(r_z + r_{p,j})^2 + r^2} \cos(\theta_\beta + \arctan r / r_z + r_{p,j}) &= H_j(\theta_\beta) \end{aligned} \right. \quad (20)
\end{aligned}$$

where $\Phi(s)$ and $H(s)$ are the moment arms of SEA and PS projected in the coronal plane. Similarly, $P_{l,inver}(s)$ describes the transfer function in inversion posture as

$$P_{l,inver}(s) = \frac{1}{I_f s^2 + k_s (\Delta l_{s,2} \Phi_2 + \Delta l_{s,3} \Phi_3)(s) + k_p (\Delta l_{p,2} H_2 + \Delta l_{p,3} H_3)(s)} \quad (21)$$

The control for the inversion consists of a feedback controller $C_{fb}^\beta(s)$ and a feedforward controller $C_{ff}^\beta(s)$, as shown in Fig. 5(b). The feedforward controller is consisted with (21). The feedback controller adopts PD controller according to the difference between the target value and the actual value.

Then, we analyze the stability of the system by Lyapunov's proof. Define the tracking error e_1 and the bionic ankle target angle θ_f^{ref} , and a switching-function-like quantity as follow:

$$\begin{cases} \theta_{f,1} = \theta_f \\ \theta_{f,2} = \dot{\theta}_{f,1} = \dot{\theta}_f \\ e_1 = K_p^\alpha \theta_f^{ref} - \theta_{f,1} \end{cases} \quad (22)$$

where K_p^α is a positive gain. Construct the Lyapunov function V_1 as

$$\begin{cases} V_1 = \frac{1}{2} e_1^2 \\ \dot{\theta}_f^{ref} - \theta_{f,2} = -K_d^\alpha e_1 \\ \dot{V}_1 = e_1 \dot{e}_1 = e_1 (\dot{\theta}_f^{ref} - \theta_{f,2}) = -K_d^\alpha e_1^2 \end{cases} \quad (23)$$

where K_d^α is a positive gain. Define the virtual control quantity $\theta_{f,2}^{ref}$ and switching-function-like quantity as follow:

$$\begin{cases} \theta_{f,2}^{ref} = \dot{\theta}_f^{ref} + K_d^\alpha e_1 \\ e_2 = \theta_{f,2}^{ref} - \theta_{f,2} \\ \dot{V}_1 = e_1 e_2 - K_d^\alpha e_1^2. \end{cases} \quad (24)$$

After substituting (19) into e_2 in (24) and converting

$$\begin{aligned}
\dot{e}_2 &= K_d^\alpha (\dot{\theta}_f^{ref} - \theta_{f,2}) \\
& - \frac{1}{I_f} \left(\tau_{dorsi} - \sum_{i=1,2} \left(k_s \left(\frac{\theta_{m,n}}{c} - f_i(\theta_{f,1}) \right) + F_T \right) \Psi_i \right. \\
& \left. - \sum_{j=1,2} k_p R_p^{-1}(\theta_{f,1}) r_{p,j} \Theta_j - F_g r_g - M_g \right) + \ddot{\theta}_f^{ref}. \quad (25)
\end{aligned}$$

Construct the Lyapunov function V_2 as

$$\begin{cases} \dot{V}_2 = V_1 + \frac{1}{2} e_2^2 \\ e_1 + \dot{e}_2 = -K_{dd}^\alpha e_2 \\ \dot{V}_2 = \dot{V}_1 + e_2 \dot{e}_2 = -K_d^\alpha e_1^2 + e_1 e_2 + e_2 e_2 \\ = -K_d^\alpha e_1^2 - K_{dd}^\alpha e_2^2 \end{cases} \quad (26)$$

where K_{dd}^α is a positive gain. Based on Lyapunov's proof of stability, PD feedback control is added. The system input τ_α for sagittal dorsiflexion can be expressed as

$$\begin{aligned}
\tau_\alpha &= I_f \left(K_p^\alpha (\theta_\alpha^{ref} - \theta_\alpha) + K_d^\alpha (\dot{\theta}_\alpha^{ref} - \dot{\theta}_\alpha) \right. \\
& \left. + K_{dd}^\alpha (\ddot{\theta}_\alpha^{ref} - \ddot{\theta}_\alpha) \right) + \tau_{dorsi} = \tau_{fb}^\alpha + \tau_{ff}^\alpha \quad (27)
\end{aligned}$$

Similarly, the input τ_β for coronal inversion was determined as

$$\begin{aligned}
\tau_\beta &= I_f \left(K_p^\beta (\theta_\beta^{ref} - \theta_\beta) + K_d^\beta (\dot{\theta}_\beta^{ref} - \dot{\theta}_\beta) \right. \\
& \left. + K_{dd}^\beta (\ddot{\theta}_\beta^{ref} - \ddot{\theta}_\beta) \right) + \tau_{inver} = \tau_{fb}^\beta + \tau_{ff}^\beta. \quad (28)
\end{aligned}$$

DOB has long been applied to industrial position control, and it is considered as an emerging control methodology for the SEA. In this article, the DOB and feedforward controller were used, as shown in Fig. 5. $P_n(s)$ is the nominal transfer function of the SEA system from the motor torque to the spring deflection as

$$P_n(s) = \frac{P_m}{1 + (k_s + k_p) P_{l,dorsi} + (k_s + k_p) P_{l,inver} + k_s P_m}(s). \quad (29)$$

By using an inverse nominal model, P_n^{-1} , the DOB preserves and enforces a dynamic response in the presence of either external disturbances or, central to the bionic ankle, motor/ankle model variations, such as changes in output joint angles. $Q(s)$ is mostly designed as a low-pass filter that makes the DOB system robust and realizable, in this case with a cut-off frequency of 10 Hz

$$Q(s) = \frac{20\pi}{s + 20\pi}. \quad (30)$$

Based on the abovementioned control model, dorsiflexion-inversion-combined 3-D ankle motion could be achieved. Substantially, all other ankle joint motions were controlled by the similar model.

IV. EXPERIMENTAL VERIFICATIONS

Four tests were conducted to verify the capabilities of the 2-DOF ankle with SEAPSSs. We measured the actual motion angle of the bionic ankle by using a Vicon motion capture system (Oxford Ltd., U.K.) at 100 Hz. Two reflective markers were placed on each SEA and PS to calculate the length change of the muscle, while four markers were placed on the foot and shank to measure the ankle angles. The ground reaction forces and moments were measured using a force plate (Kistler, Switzerland) at 1 kHz. In order to ensure repeatability and accuracy of ankle movement, all the experiments were repeated ten times, with the average given. The root-mean-square error (RMSE) was also used to compare the difference between the measured and idealized values.

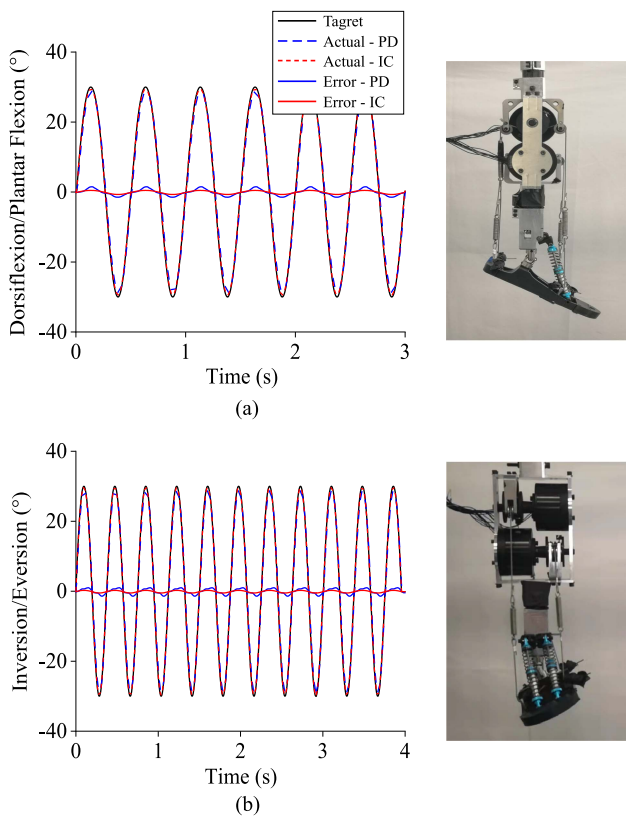


Fig. 6. 2-D motion tracking of dorsiflexion/plantar flexion (a) and inversion/eversion (b) of the bionic ankle. IC, impedance controller.

A. 2-D Ankle Joint Motion Tracking

We evaluated the motion performance of the bionic ankle by comparing actual trajectories measured by the Vicon system with target trajectories. The mini-jerk quintic polynomial was used to plan the target trajectory of the ankle joint in the sagittal and frontal planes. In the impedance controller, K_p^α , K_d^α , and K_{dd}^α were set to 0.11, 0.025, and 0.008, respectively, while K_p^β , K_d^β , and K_{dd}^β were set to 0.15, 0.033, and 0.006, respectively. These values were determined referring to the PID tuning method in MATLAB. Meanwhile, we exploited multisectional PD control to achieve stable motions by using a trial and error process. Each of the four motions (plantar flexion, dorsiflexion, inversion, eversion) was divided into ten subsections, and each subsection used different control gains to fit the target values. It is assumed that the errors between the target and actual values are in a similar range, then the multisectional K_p and K_d can be used to simulate the nonlinear joint stiffness. Through the actual angle value returned by the sensor, the corresponding K_p and K_d values were determined. Finally, K_p ranges from 0.11 to 0.87 while K_d changes from 0.01 to 0.11.

For 2-D motion, the ankle was rotated about the x -axis with $\theta_\alpha = \pm 30^\circ$ (2 Hz), and about the y -axis with $\theta_\beta = \pm 30^\circ$ (2.5 Hz). These two motions cover the entire range of motion in the sagittal and frontal planes. Fig. 6 and Video 1 show the 2-D motion tracking trajectories. The maximum errors between the target and actual trajectory are smaller than 1.2° (4.0%)

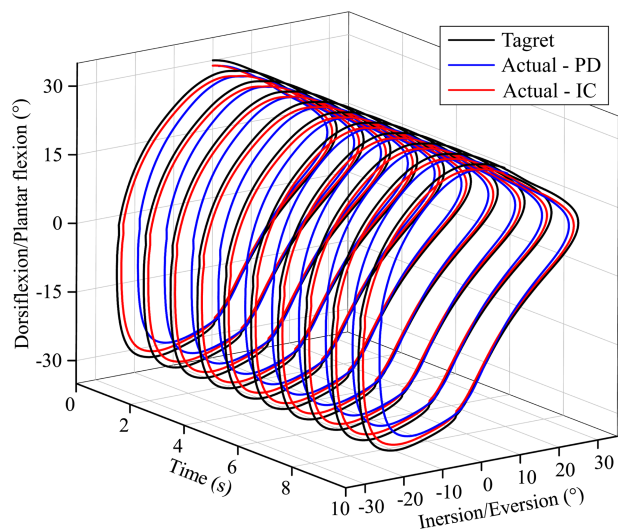


Fig. 7. 3-D motion tracking of the bionic ankle. IC, impedance controller.

in the sagittal plane and 0.9° (3.0%) in the frontal plane with the PD controller, while these errors reduced to 0.2° (0.7%) in the sagittal plane and 0.3° (1.0%) in the frontal plane with the impedance controller. The percentage values in 2-D/3-D motion tracking were calculated as the absolute errors divided by the target values.

B. 3-D Ankle Joint Motion Tracking

The trajectory of the spatial 3-D planning is from dorsiflexion to eversion, eversion to plantar flexion, plantar flexion to inversion, inversion to dorsiflexion, and so on. All motions have an amplitude of 30° (1 Hz). Fig. 7 and Video 1 shows the motion tracking performance when the ankle rotates in three dimensions. The maximum errors between the target and actual ankle trajectories are smaller than 2.7° (9.0%) under the PD controller and 0.7° (2.3%) under the impedance controller. Then, the bionic ankle was then validated by comparing the measured 3-D time-angle trajectories with those of the human ankle under natural walking gait (see Fig. 8 and Table II). We can see that the similarity between them is quite high with relative RMSE well below 4.2% with the PD controller and 1.0% with the impedance controller. Finally, the 2-D/3-D motion tracking performance of the bionic ankle were listed in Table II, all of which showed good agreement with the target values. This suggests that the bionic ankle can meet the motion requirements in both planes.

C. Ankle Stiffness

During one complete gait cycle on the ground, human ankle stiffness is adaptable. The joint stiffness of the bionic ankle under different loading conditions was tested using a universal testing machine [see Fig. 9(a)]. The lower leg was firmly attached, and the foot was in close contact with a metal plate connected to the sensor, for measuring the actual output torque of the ankle. Fig. 9(b) shows the relationship between the ankle torque and

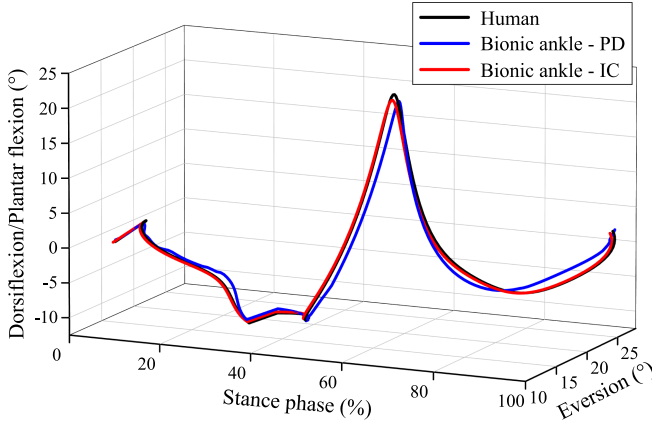


Fig. 8. Comparison of the 3-D time-angle trajectories between the bionic ankle and the human ankle [34] during stance phase of normal walking. IC, impedance controller.

TABLE II
MOTION TRACKING PERFORMANCE OF THE BIONIC ANKLE

Name	2-D		3-D	
	Dorsiflexion /Plantar flexion	Inversion /Eversion	Circle	Human walking
Target angle	$\pm 30^\circ$	$\pm 30^\circ$	$\pm 30^\circ$	-10° – 24° (D/P) 12° – 26° (I/E)
Measured angle	PD	-28.8° – 29.0°	$\pm 29.1^\circ$	-9.9° – 22.7° (D/P) 12.4° – 25.0° (I/E)
	IC	$\pm 29.8^\circ$	$\pm 29.7^\circ$	-10° – 23.5° (D/P) 11.7° – 25.8° (I/E)
Max. error	PD	1.2°	0.9°	2.7°
	IC	0.2°	0.3°	0.7°
Relative max. error	PD	4.0%	3.0%	9.0%
	IC	0.7%	1.0%	2.3%
RMSE	PD	1.0°	0.8°	2.1°
	IC	0.1°	0.2°	0.4°
Relative RMSE	PD	3.3%	2.7%	7.0%
	IC	0.3%	0.7%	1.3%

Mean values are depicted ($n = 10$) for the measured angle and the errors. Human walking data are depicted by dorsiflexion/plantar flexion (D/P) and inversion/eversion (I/E). RMSE ($n = 10$) is calculated between the target and measured time trajectories of the motion. IC, impedance controller.

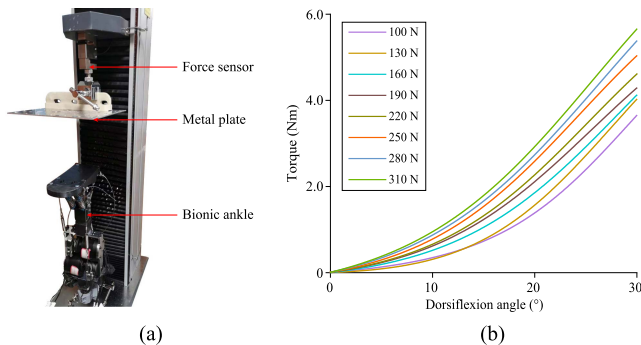


Fig. 9. Ankle stiffness estimated as an approximation of measured angle-torque curves. (a) Experimental setups. (b) Angle-torque trajectories under different SEA tensile forces.

the joint angle under dorsiflexion at different SEA tensile forces. Generally, a nonlinear joint stiffnesses can be obtained when the ankle angle changes. As the dorsiflexion angle increases, the ankle stiffness increases. The ankle torque increases linearly with the angle above 15° . Varying joint stiffness driven by the

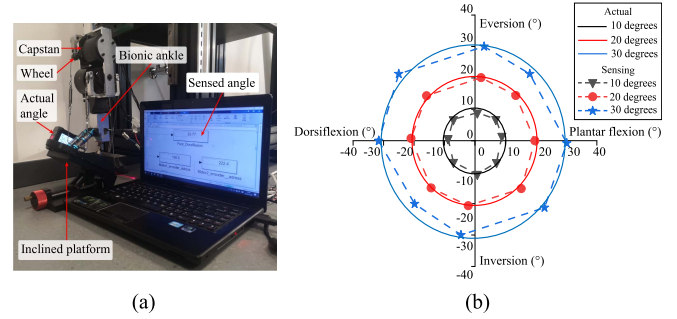


Fig. 10. Sensing the ankle angle on different slope surface. (a) Experimental setups. (b) Angles sensed by the bionic ankle under various postures.

SEAPS allows the robot to maintain balance when walking on different road conditions.

D. Ankle Angle Sensing

To verify the adaptability of the bionic ankle in unstructured terrain, the test of sensing a tilted platform without any sensors was designed [see Fig. 10(a)]. The bionic ankle was placed on the top of the platform, and the actual tilting angle of this platform was measured by a digital inclinometer (SYNTEK, China). The surface of the platform is flat and the footplate can be fully placed on the surface. By changing the positions of the platform, we can set the ankle postures to 1-DOF dorsi/plantar flexion or inversion/eversion, as well as 2-DOF motion combining them. By adjusting the tilting angle of the platform, the ankle angle in the certain posture changes accordingly (Video 2). The capstans connected to the motors rotate as the length of the SEAs fixed at the ankle changes. The feedback from the motor encoder is used to calculate the length change of the SEA. Based on the kinematic model in Section II, the bionic ankle can then sense the actual road conditions in terms of tilting angle. Fig. 10(b) shows the comparisons between the angle sensed by the ankle and the measured actual tilting angle of the platform. The maximum error is 6.7% and the minimum error is 0.5% when the test road angle is 20° and 30° . The bionic ankle has good sensing ability on even terrain in this angle range. But when the test road angle is 10° , the maximum error is increased to 11.2%. This increased error may be induced from the fact that the bionic ankle senses the road angle based on the motor encoder, which has an enlarged error of predicted SEA deformation in the case of small range of motor rotation.

E. Land Buffering Capacity

Whether bipeds or humans, landing from a high place brings a huge amount of impact. We conducted a series of real-world experiments to investigate the land buffering properties of the bionic ankle at various poses (see Fig. 11 and Video 3). The ankle was placed at 40-cm high, and vertically dropped to a 22° tilted platform by a linear guide rail [see Fig. 11(c)]. The surface here was different from that in the angle sensing test, with uneven terrain. The pressure sensor was used to disable the motors after landing so that the footplate could be fully attached

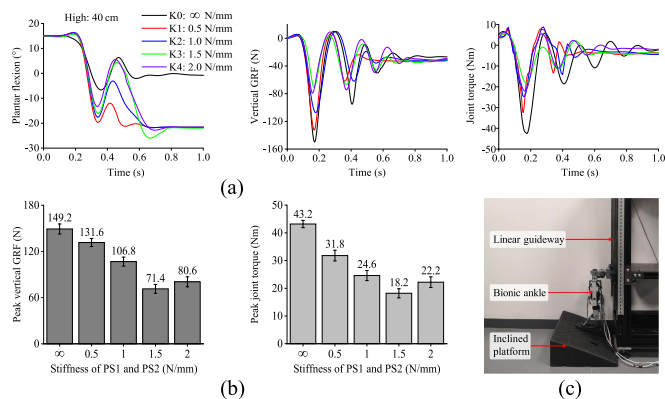


Fig. 11. (a) Ankle angle, vertical GRF, joint torque with different PS stiffnesses under impact in plantar flexion. The bionic ankle was subjected to free fall impact from 40-cm above the ground with plantar flexion posture. (b) Mean \pm standard deviations of peak vertical GRF and peak joint torque. (c) Experimental setups of the land buffering test.

to the platform. The use of this pressure sensor is only necessary for the landing experiment. The ankle angles and force plate data were collected during each test, while the length changes of the SEAs and PSs were calculated. The dynamic model in Section II are used to calculate the change in ankle joint torque under various states of impact. Combining the measured vertical ground reaction force (GRF) during landing, the buffering effect of the bionic ankle is analyzed. The stiffness of PS1 and PS2 was changed from 0.5 to 2.0 N/mm. To verify the effect of the PSs on the buffering performance, no spring (infinite stiffness) under plantar flexion was defined as the reference to compare all the tests under dorsi/plantar flexion.

Fig. 11 shows the variations of the ankle angle, vertical GRF, and joint torque during landing under different PS stiffnesses with an initial 15° plantar flexion angle. When the stiffness is infinite, the peak vertical GRF is 149.2 N and the peak joint torque is 43.2 Nm. The impact lasts for 0.8 s before completely disappearing. The bionic ankle reached to the equilibrium state in 0.42 s with PSs of 0.5 N/mm, much quicker than 0.81 s of no PS. Compared with no spring, the peak vertical GRF were reduced by 11.8%, 28.4%, 52.2%, and 46.0% at spring stiffnesses of 0.5, 1.0, 1.5, and 2.0 N/mm, respectively. The peak ankle torques were reduced by 26.4%, 43.1%, 57.9%, and 48.6%, respectively. With increasing spring stiffness, the buffering rate (reduction in peak vertical GRF and joint torque) first increased and then decreased, while the maximum rate occurred under the stiffness of 1.5 N/mm. This is because that with too stiff PSs, the springs cannot be fully compressed to absorb energy during landing, resulting in decreased buffering.

Since the bionic ankle joint cannot perform dorsiflexion when the stiffness is infinite, the other four spring stiffnesses from 0.5 to 2.0 N/mm are used for testing the landing buffer under dorsiflexion with an initial angle of 15° (see Fig. 12). The results showed that there was no obvious difference in the dorsiflexion angle of the ankle joint under different stiffnesses. After landing, the ankle joint reached to the stationary state in 0.39 s at spring stiffnesses of 0.5 N/mm. Compared with no spring in plantar flexion, the peak vertical GRFs and peak ankle joint torques were

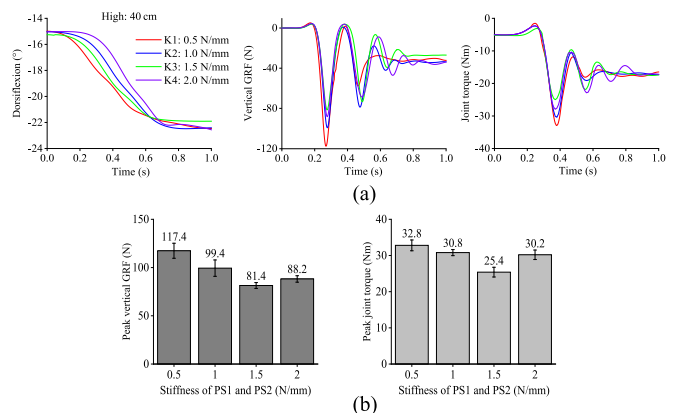


Fig. 12. (a) Ankle angle, vertical GRF, joint torque with different PS stiffnesses under impact in dorsiflexion. The bionic ankle was subjected to free fall impact from 40-cm above the ground with dorsiflexion posture. (b) Mean \pm standard deviations of peak vertical GRF and peak joint torque.

TABLE III

PEAK VERTICAL GRF AND JOINT TORQUE USING DIFFERENT PS STIFFNESS

Peak value	Ankle posture	PS1 and PS2 (N/mm)				
		∞	0.5	1	1.5	2
Vertical GRF (N)	Plantar flexion	149.2	131.6	106.8	71.4	80.6
	Dorsiflexion	/	117.4	99.4	81.4	88.2
Reduction (%)	Plantar flexion	0	11.8	28.4	52.2	46.0
	Dorsiflexion	/	21.3	33.4	45.4	40.9
Joint torque (Nm)	Plantar flexion	43.2	31.8	24.6	18.2	22.2
	Dorsiflexion	/	32.8	30.8	25.4	30.2
Reduction (%)	Plantar flexion	0	26.4	43.1	57.9	48.6
	Dorsiflexion	/	24.1	28.7	41.2	30.1

Mean values are depicted ($n = 10$). No spring (infinite stiffness) under plantar flexion was used as the baseline for all the tests.

all reduced at spring stiffnesses of 0.5, 1.0, 1.5, and 2.0 N/mm. However, the cushioning effect under dorsiflexion is slightly lower than that under plantar flexion. Finally, the peak vertical GRFs and peak joint torques using different PS stiffness under dorsi/plantar flexion were listed in Table III.

In addition, the bionic ankle with an initial 15° eversion angle was tested. As shown in Fig. 13, under different stiffnesses from 0.5 to 2.0 N/mm, the time from impact to the stationary state is almost 0.38 s. At stiffness of 0.5 N/mm, the maximum peak vertical GRF of 183.8 N occurs, corresponding to the maximum peak ankle joint torque of 48.6 Nm. With the PSs stiffness of 2 N/mm, the maximum peak vertical GRF of 131.8 N and maximum peak ankle joint torque of 41.8 Nm were observed. Different with other two postures, the buffering effect of the bionic ankle decreases with the increase in spring stiffness.

V. DISCUSSION

This article presents a 2-DOF active bionic ankle composed of four SEAPs with distinct land buffering capability. Three unique features are presented: 1) A multi-axial mechanism including four SEAPs allows a wide range of motion (WROM) in both the sagittal and frontal planes, i.e., 2-DOF $\pm 30^\circ$, which covers most of the human ankle motions. 2) The sensing ability on an even terrain through a kinematic model shows that it has the potential of adapting to various road conditions. 3) The SEAPs

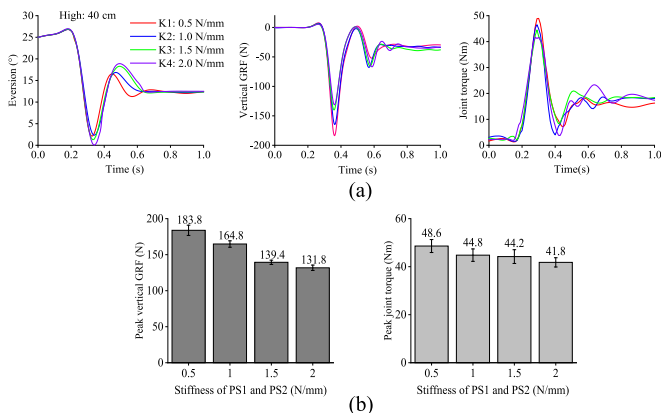


Fig. 13. (a) Ankle angle, vertical GRF, joint torque with different PS stiffnesses under impact in eversion. The bionic ankle was subjected to free fall impact from 40-cm above the ground with eversion posture. (b) Mean \pm standard deviations of peak vertical GRF and peak joint torque.

structure provides a landing buffer that is able to reduce vertical GRF and joint torque when the bionic ankle vertically falls from high places. To the best of our knowledge, this is the first time that SEAPSs have been applied to investigate the adaptability of a 2-DOF active ankle over a WROM, aiming to ease the tradeoff between land impact and stiffness diversity. However, there are some questions need to be investigated. We draw a few points to discuss and some future prospects below.

A. 2-DOF Over a WROM With SEAPSs

All analysis and tests presented in this study were performed with two motors driving four SEAPSs to achieve 2-DOF for the bionic ankle. As a result, the ankle can achieve a range of motion of 30° in both the sagittal and frontal planes. This allows the robot to better adapt to complex road conditions. In terms of bionic ankles, the concept of SEAPS has been studied for decades. Bionic prostheses were developed to mimic the function of a biological ankle during level-ground walking [35], reduces motor torque, stores and returns energy, and reduces peak impact force [36], [37]. These studies show the superiority of SEAPS in the use of bionic ankle joints. But all of them include motion in the sagittal plane only. Most SEAPS mechanisms adopt SEA1 and PS1 parallel connection modes. In this study, PS3 and PS4 springs are added based on PS1 and PS2 to increase the range of motion and make two PSs always store energy, while the other PSs release energy when the ankle joint switches from one posture to another.

To date, only one application of SEAPSs has been found in a bionic ankle with 2-DOF, which provides a powered DOF for dorsi/plantar flexion and a passive DOF for inversion/eversion: 22° in plantar flexion, 18° in dorsiflexion, 20° in inversion and eversion, a weight of 2.95 kg, and a height of 43 cm [33]. In this study, we have improved the ankle design to make both the 2 DOFs active, while the range of motion in both planes are increased to $\pm 30^\circ$ compared with traditional robotic ankles using elastic elements.

B. Joint Stiffness Changes and Adaptive Capabilities

A bionic robotic ankle needs push-off to enable it to lift its leg after it adapts to complex road conditions. Joint stiffness becomes a key characteristic of foot-ground interaction. This study shows that the stiffness of the human ankle can be simulated by applying SEAPS to a bionic ankle. This was also confirmed in an earlier study of a powered ankle prosthesis composed of SEAPSs [38]. The adaptive ability of the robotic ankle has become a research hotspot in recent years [19], [39], [40]. In this article, it is proposed for maybe the first time to judge adaptability through the sensing ability of inclined terrains. The kinematic model is used to calculate the feedback values of two motor encoders in the sensing test. Then, the ankle angles can be estimated simultaneously. After comparing the sensed angle with the actual platform angle, it can be found that the accuracy between them reaches more than 93% when the test road angles are 20° and 30° .

Next is to analyze why the ankle can best adapt in this region. Four SEAPSs enable the bionic ankle to have the corresponding elastic force generated by the PSs acting on the footplate regardless of the posture. As the angle of the test platform increases, the elasticity generated by the PSs increases, which can promote the foot to better adapt to the platform.

C. Landing Buffer of the Bionic Ankle

The results of this investigation highlight the importance of the SEAPS at different stiffnesses for the avoidance of impact loads and adaptive performance of the bionic ankle in collision with complex road conditions. When the bionic ankle vertically hits an inclined road with different postures, the SEAPS reduces its impact with the surface inconsistently. Among them, the cushioning of the ankle in plantar flexion pose is the best (up to 52.2% and 57.9% reduction in vertical GRF and joint torque, respectively). The deformations of the SEAPSs after landing under dorsiflexion/plantar flexion are larger than that under inversion/eversion, which helps the bionic ankle absorb more impact energy and generate less impact force. A study of a SEAPS-powered ankle prosthesis walking on flat terrain found a maximum reduction of 11% in peak resultant GRF force [35].

With the increase in spring stiffness, the cushioning effect first increases and then decreases. With a too rigid spring, the foot does not deform well when in contact with the ground, as seen from changes in joint angles. Therefore, as the spring stiffness increases larger than a critical value, the cushioning effect decreases. In addition to the impact, the proper spring stiffness is also a great help to very fast adapt to inclined road.

D. Limitations and Future Works

From the mechanical application: ① For robots, lightweight is one of the common requirements. However, the combined weight of the two motors used in this article is 860 g, which makes the bionic ankle quite heavy overall. ② The bottom of the footplate design is flat, so the ankle angle sensing requires the flatness of the road surface to be fully attached by the footplate. From the system integration: The 2-DOF active ankle with four

SEAPs can improve the land buffering performance in sloping road conditions at the cost of mass and structural complexity.

In future, we intend to first improve the bionic ankle by selecting more advanced motor with less weight, smaller size, and higher power density ratio. The second step is to characterize and quantify the impedance and bandwidth limits of the bionic ankle for carefully defined tasks, such as applying a 100-N force on the front edge of the footplate and recording the ankle joint trajectory. Finally, the proposed ankle should be applied on real robot, maybe first on the jumping robot, as it can store energy for the next jumping cycle during landing by using SEAPs.

VI. CONCLUSION

In this article, we proposed a 2-DOF bionic ankle with distinct land buffering property. Four SEAPs mimic the biomechanics of the muscles surrounding the human ankle. Two motors can simultaneously drive the ankle to increase the motor capacity. Kinematic analysis showed that a wide range of motion has been achieved in both dorsi/plantar flexion and inversion/eversion. The ankle joint stiffness can adapt to various loading conditions, which reproduces the trend of the human ankle and helps the gait of the robotic ankle. Road sensing tests show that the bionic ankle has good adaptability in both sagittal and frontal planes. Another finding is that SEAPs can reduce the landing impact in complex road conditions. The buffering performance with different PS stiffnesses and postures were evaluated. The results showed that the ankle has the best cushioning effect under plantar flexion, and a proper PS stiffness can satisfy both the buffering effect and adaptive speed during landing. This study gives an inspiration of using SEAPs-based mechanism in robotic ankle design. It exhibits high land buffering performance in an unstructured environment, and can well mimic the human ankle movement in terms of complex 3-D motions.

REFERENCES

- [1] A. J. Ijspeert, "Biorobotics: Using robots to emulate and investigate agile locomotion," *Science*, vol. 346, no. 6206, pp. 196–203, Oct. 2014.
- [2] S. M. Colby, R. A. Hintermeister, M. R. Torry, and J. R. Steadman, "Lower limb stability with ACL impairment," *J. Orthopaedic Sports Phys. Ther.*, vol. 29, no. 8, pp. 444–451, Aug. 1999.
- [3] S. E. Ross and K. M. Guskiewicz, "Examination of static and dynamic postural stability in individuals with functionally stable and unstable ankles," *Clin. J. Sport Med.*, vol. 14, no. 6, pp. 332–338, Nov. 2004.
- [4] Z. Q. Zhang, J. L. Yang, and H. Yu, "Effect of flexible back on energy absorption during landing in cats: A biomechanical investigation," *J. Bionic Eng.*, vol. 11, no. 4, pp. 506–516, Oct. 2014.
- [5] E. Azizi, N. P. Larson, E. M. Abbott, and N. Danos, "Reduce torques and stick the landing: Limb posture during landing in toads," *J. Exp. Biol.*, vol. 217, no. 20, pp. 3742–3747, Oct. 2014.
- [6] K. E. Paskins, A. Bowyer, W. M. Megill, and J. S. Scheibe, "Take-off and landing forces and the evolution of controlled gliding in northern flying squirrels *Glaucomys sabrinus*," *J. Exp. Biol.*, vol. 210, no. 8, pp. 1413–1423, Apr. 2007.
- [7] I. L. Wang et al., "Influences of different drop height training on lower extremity kinematics and stiffness during repetitive drop jump," *Appl. Bionics Biomech.*, vol. 2021, Mar. 2021, Art. no. 5551199.
- [8] C. O. Kean, *Comparison of Static and Dynamic Balance Training on Muscle Activation, Static Balance, Jumping and Sprint Performance*. St. John's, NL, Canada: Memorial Univ. of Newfoundland, 2005.
- [9] J. L. R. Jayalath, M. de Noronha, N. Weerakkody, and R. Bini, "Effects of fatigue on ankle biomechanics during jumps: A systematic review," *J. Electromyography Kinesiology*, vol. 42, pp. 81–91, Oct. 2018.
- [10] K. Radkhah, C. Maufroy, M. Maus, D. Scholz, A. Seyfarth, and O. von Stryk, "Concept and design of the biobiped1 robot for human-like walking and running," *Int. J. Hum. Robot.*, vol. 8, no. 3, pp. 439–458, Sep. 2011.
- [11] B. Vanderborght, N. G. Tsagarakis, R. Van Ham, I. Thorson, and D. G. Caldwell, "MACCEPA 2.0: Compliant actuator used for energy efficient hopping robot Chobino1D," *Auton. Robot.*, vol. 31, no. 1, pp. 55–65, Jul. 2011.
- [12] F. Guenther and F. Iida, "Energy-efficient monopod running with a large payload based on open-loop parallel elastic actuation," *IEEE Trans. Robot.*, vol. 33, no. 1, pp. 102–113, Feb. 2017.
- [13] J. Zhao, T. Zhao, N. Xi, M. W. Mutka, and L. Xiao, "MSU tailbot: Controlling aerial maneuver of a miniature-tailed jumping robot," *IEEE/ASME Trans. Mechatron.*, vol. 20, no. 6, pp. 2903–2914, Dec. 2015.
- [14] D. E. Lieberman et al., "Foot strike patterns and collision forces in habitually barefoot versus shod runners," *Nature*, vol. 463, no. 7280, pp. 531–535, Jan. 2010.
- [15] K. A. Webster, B. G. Pietrosimone, and P. A. Gribble, "Muscle activation during landing before and after fatigue in individuals with or without chronic ankle instability," *J. Athletic Training*, vol. 51, no. 8, pp. 629–636, Aug. 2016.
- [16] L. Y. T. Chan, Y. T. N. Sim, F. K. Gan, and H. R. Bin Abd Razak, "Effect of chronic ankle instability on lower extremity kinematics, dynamic postural stability, and muscle activity during unilateral jump-landing tasks: A systematic review and meta-analysis," *Phys. Ther. Sport*, vol. 55, pp. 176–188, May 2022.
- [17] G. Chen, P. Qi, Z. Guo, and H. Y. Yu, "Mechanical design and evaluation of a compact portable knee-ankle-foot robot for gait rehabilitation," *Mech. Mach. Theory*, vol. 103, pp. 51–64, Sep. 2016.
- [18] A. Mazumdar et al., "Parallel elastic elements improve energy efficiency on the STEPPR bipedal walking robot," *IEEE/ASME Trans. Mechatron.*, vol. 22, no. 2, pp. 898–908, Apr. 2017.
- [19] Z. Qaiser, L. P. Kang, and S. Johnson, "Design of a bioinspired tunable stiffness robotic foot," *Mech. Mach. Theory*, vol. 110, pp. 1–15, Apr. 2017.
- [20] W. Roozing, Z. Y. Ren, and N. G. Tsagarakis, "An efficient leg with series-parallel and biarticular compliant actuation: Design optimization, modeling, and control of the eLeg," *Int. J. Robot. Res.*, vol. 40, no. 1, pp. 37–54, Jan. 2021.
- [21] G. A. Pratt and M. W. Williamson, "Series elastic actuators," in *Proc. IEEE/RSJ Int. Conf. Intell. Robots Syst.*, 1995, vol. 1, pp. 399–406.
- [22] Y. Zhao, N. Paine, S. J. Jorgensen, and L. Sentis, "Impedance control and performance measure of series elastic actuators," *IEEE Trans. Ind. Electron.*, vol. 65, no. 3, pp. 2817–2827, Mar. 2018.
- [23] U. Mettin, P. X. La Hera, L. B. Freidovich, and A. S. Shiriaev, "Parallel elastic actuators as a control tool for preplanned trajectories of underactuated mechanical systems," *Int. J. Robot. Res.*, vol. 29, no. 9, pp. 1186–1198, Aug. 2010.
- [24] W. R. Brown and A. G. Ulsoy, "A maneuver based design of a passive-assist device for augmenting active joints," *J. Mech. Robot.*, vol. 5, no. 3, Aug. 2013, Art. no. 031003.
- [25] J. Borras and A. M. Dollar, "Actuation torque reduction in parallel robots using joint compliance," *J. Mech. Robot.*, vol. 6, no. 2, Jun. 2014, Art. no. 021006.
- [26] Y. Zhu, J. Yang, H. Jin, X. Zang, and J. Zhao, "Design and evaluation of a parallel-series elastic actuator for lower limb exoskeletons," in *Proc. IEEE Int. Conf. Robot. Automat.*, 2014, pp. 1335–1340.
- [27] C. Hong, D. W. Tang, Q. Q. Quan, Z. Q. Cao, and Z. Q. Deng, "A combined series-elastic actuator & parallel-elastic leg no-latch bio-inspired jumping robot," *Mech. Mach. Theory*, vol. 149, Jul. 2020, Art. no. 103814.
- [28] J. Schonherr, M. Muller, and B. Glasmacher, "Concept, design and construction of an active supporting foot prosthesis," *Biomed. Eng.-Biomed. Tech.*, vol. 59, Oct. 2014, Art. no. S1136.
- [29] T. Jung, J. Lim, H. Bae, K. K. Lee, H.-M. Joe, and J.-H. Oh, "Development of the humanoid disaster response platform DRC-HUBO," *IEEE Trans. Robot.*, vol. 34, no. 1, pp. 1–17, Feb. 2018.
- [30] S. Kuindersma et al., "Optimization-based locomotion planning, estimation, and control design for the atlas humanoid robot," *Auton. Robot.*, vol. 40, no. 3, pp. 429–455, Mar. 2016.
- [31] B. S. Vinay et al., "Design and structural analysis of a passive ankle-foot prosthesis with manually adjustable stiffness and having two degrees of freedom," *Mater. Today-Proc.*, vol. 65, pp. 3496–3505, 2022.
- [32] W.-S. Jang, D.-Y. Kim, Y.-S. Choi, and Y.-J. Kim, "Self-contained 2-DOF ankle-foot prosthesis with low-inertia extremity for agile walking on uneven terrain," *IEEE Robot. Automat. Lett.*, vol. 6, no. 4, pp. 8134–8141, Oct. 2021.

- [33] A. Agboola-Dobson, G. W. Wei, and L. Ren, "Biologically inspired design and development of a variable stiffness powered ankle-foot prosthesis," *J. Mech. Robot.*, vol. 11, no. 4, Aug. 2019, Art. no. 041012.
- [34] L. Ren, R. K. Jones, and D. Howard, "Whole body inverse dynamics over a complete gait cycle based only on measured kinematics," *J. Biomech.*, vol. 41, no. 12, pp. 2750–2759, Aug. 2008.
- [35] A. M. Grabowski and S. D'Andrea, "Effects of a powered ankle-foot prosthesis on kinetic loading of the unaffected leg during level-ground walking," *J. Neuroeng. Rehabil.*, vol. 10, Jun. 2013, Art. no. 49.
- [36] M. F. Eilenberg, H. Geyer, and H. Herr, "Control of a powered ankle-foot prosthesis based on a neuromuscular model," *IEEE Trans. Neural Syst. Rehabil. Eng.*, vol. 18, no. 2, pp. 164–173, Apr. 2010.
- [37] H. M. Herr and A. M. Grabowski, "Bionic ankle-foot prosthesis normalizes walking gait for persons with leg amputation," *Proc. Roy. Soc. Biol. Sci.*, vol. 279, no. 1728, pp. 457–464, Feb. 2012.
- [38] S. K. Au, J. Weber, and H. Herr, "Powered ankle-foot prosthesis improves walking metabolic economy," *IEEE Trans. Robot.*, vol. 25, no. 1, pp. 51–66, Feb. 2009.
- [39] J. W. Sun, G. S. Song, J. K. Chu, and L. Q. Ren, "An adaptive bioinspired foot mechanism based on tensegrity structures," *Soft Robot.*, vol. 6, no. 6, pp. 778–789, Dec. 2019.
- [40] M. G. Catalano et al., "Adaptive feet for quadrupedal walkers," *IEEE Trans. Robot.*, vol. 38, no. 1, pp. 302–316, Feb. 2022.



Shun Zhao received the B.S. degree in mechanical design, manufacturing, and automation from Ludong University, Yantai, China, in 2015, and the M.S. degree in mechanical engineering from Changan University, Xi'an, China, in 2018. He is currently working toward the Ph.D. degree in bionic science and engineering with Jilin University, Changchun, China.

His research interests include robotics and biomechanics.



Wei Liang received the B.S. degree in mechanical engineering and automation from Hunan Institute of Science and Technology, Yueyang, China, in 2014, and the M.S. and Ph.D. degrees in bionic science and engineering from Jilin University, Changchun, China, in 2016 and 2020, respectively.

He is currently a Postdoctoral Researcher with Jilin University, Changchun, China. His research interests include knee prosthesis, biomechanics, and legged robotics.



Kunyang Wang (Member, IEEE) received the B.S. and M.S. degrees in mechanical engineering from Harbin Institute of Technology, Harbin, China, in 2012 and 2014, respectively, and the Ph.D. degree in mechanical engineering from the University of Manchester, Manchester, U.K., in 2019.

Since 2021, he has been an Associate Professor with Jilin University, China. His current research interests include human biomechanics, bioinspired robotics, mechatronics, prosthetics,

and healthcare devices.

Dr. Wang is currently a Member of American Society of Mechanical Engineers and International Society of Bionic Engineering.



Lei Ren (Member, IEEE) received the B.S. and M.S. degrees in mechanical engineering and the Ph.D. degree in vehicle engineering from Jilin University, Changchun, China, in 1994, 1997, and 2000, respectively, and the Ph.D. degree in biomechanics from University of Salford, Manchester, U.K., in 2005.

He is currently a Reader with University of Manchester, Manchester, U.K., and a Professor with Jilin University, Changchun, China. His research interests include biomechanics, bionic healthcare engineering, and biorobotics.

Dr. Ren is currently an Associate Editor of *Frontiers in Bioengineering and Biotechnology*, the Editorial Board Members of *Journal of Bionic Engineering*, and *PLoS One*.



Zhihui Qian received the Ph.D. degree in bionic science and technology from Jilin University, Changchun, China, in 2010.

He is currently a Professor with Jilin University, Changchun, China. His research interests include human biomechanics, innovative bionic robotics, and bionic healthcare engineering.

Dr. Qian is the Founding Member of the International Society of Bionic Engineering.



Guangrong Chen received the B.Eng. degree in automation from the Beijing Institute of Technology, Beijing, China, in 2012, and the Ph.D. degree in control science and engineering from the Beijing Institute of Technology, Beijing, China, in 2018.

He was a lecturer with the Robotics Research Center, Beijing Jiaotong University, Beijing, China, in 2018, and is currently a Vice Professor. His research interests include robotics and artificial intelligence.

Dr. Chen is currently a member of Chinese Association of Automation Society.



Xuewei Lu received the B.S. degree in mechanical engineering from Wuhan University of Technology, Wuhan, China, in 2013, the M.S. degree in mechanical engineering from the University of Dundee, Dundee, U.K., in 2014, and the Ph.D. degree in mechanical engineering from the University of Manchester, Manchester, U.K., in 2022.

She is currently a Postdoctoral Researcher with Jilin University, Changchun, China. Her current research interests include walking bipeds,

bioinspired robots, and human biomechanics.



Di Zhao received the Ph.D. degree in automotive engineering from Jilin University, Changchun, China, in 2020.

He is currently a Postdoctoral Researcher with Jilin University, Changchun, China. His current research interests include robotic control, autonomous vehicle control, racecar vehicle dynamic control, and drive-by-wire chassis control.



Xu Wang received the B.S. degree in mechanical engineering and automation from Zhengzhou University, Zhengzhou, China, in 2013, and the M.S. degree in mechanical design and theory in 2017 from Jilin University, Changchun, China, where he is currently working toward the Ph.D. degree in bionic science and engineering.

His current research interests include design and control of knee prosthesis, biomechatronic, and robotics.



Luquan Ren received the B.S. and M.S. degrees in tractor from Jilin University of Technology, Changchun, China, in 1967 and 1981, respectively.

Since 2007, he has been a Member of the Chinese Academy of Sciences. He is currently a Professor with Jilin University, Changchun, China. His current research interests include bionic design and manufacturing, the basic theory of engineering bionics such as bionic health-care engineering, bionic robotics, and intelligent

prostheses.

Prof. Ren is currently the Editor-in-Chief of International Journal of Bionic Engineering, the Standing Vice President of the International Society of Bionic Engineering.